



Fabrication, characterization and excellent formaldehyde gas sensing of Tb-doped In_2O_3 beaded-porous nanotubes

Haojie Duan¹ · Yue He¹ · Shouchun Li¹ · Li Liu¹ · Suyang Xu² · Yu Li¹ · Haiying Li¹ · Yimin Gong¹ · Qingcheng Liang³ · Yali Cheng¹

Received: 15 June 2018 / Accepted: 7 September 2018 / Published online: 14 September 2018
© Springer Science+Business Media, LLC, part of Springer Nature 2018

Abstract

The pure and Tb-doped In_2O_3 beaded-porous nanotubes (BPNTs) are fabricated by simple electrospinning method. The crystal phase, morphology and chemical composition of the obtained samples were analyzed by characteristic techniques (XRD, FE-SEM, TEM, EDS, XPS, etc.). The mechanism of forming BPNTs structure was studied, and phase separation plays a key role in the process of formation. A series of sensing tests toward formaldehyde gas showed that 6 mol% Tb-doped In_2O_3 BPNTs exhibited the best sensing performance: high response (75–50 ppm), shorter response and recovery times (2 s and 12 s), low limit of detection (LOD, 1.27–100 ppb), good selectivity and long-term stability, etc. The significantly improved gas sensing properties were mainly resulted from their high surface basicity, enriched defects (oxygen vacancies), small crystallite size and complex porous structures.

1 Introduction

Air pollution, as a global environmental problem, has caused significant harm to people's health. Especially for formaldehyde gas, it is a naturally occurring organic compound which has a pungent irritating odor. Exposure is mainly via the inhalation of vapors and can be known to cause headaches, difficulty breathing and burning in the throat [1, 2]. The growing awareness of air pollution and the popular of domestic intelligent detection equipment are driving the demand for gas sensors. Semiconductor gas sensors provide a promising approach for low cost, compact size, and high accuracy. In_2O_3 , as one n-type oxide semiconductor, has been frequently used to detect various flammable and toxic

gases because of wide band gap (3.5–3.75 eV), good thermal stability, chemical stability, high electrical conductivity and lattice defects [3, 4]. The defects are associated with oxygen vacancies, and oxygen vacancies serving as active site for absorbing oxygen species is absolutely critical to gas sensing properties [5]. In particular, the donor level introduced by oxygen vacancies provides free electrons to the conduction band of the semiconductor and then transfer to oxygen species on the surface of In_2O_3 . However, some inherent weaknesses of pure In_2O_3 sensor such as low response and poor selectivity may hamper the practical application. Hence, many researches have been carried out to further enhance sensing performance. In summary, there two major method: increasing contact surface and doping other ions or crystal phase [6, 7]. Generally speaking, larger surface area can provide more action site for oxygen species and lead to more electrons absorbed on the surface of samples. various In_2O_3 structures have been synthesized such as nanoparticles [6], nanowires [8], nanosheets [9] and nanospheres [10], etc. For instance, Hu et al. prepared In_2O_3 hollow microtubules by using degreasing cotton as soft bio-templates, the result indicated that Cl_2 sensing properties were remarkably enhanced in sensitivity and selectivity compared with In_2O_3 particles [11]. For another method (introducing other ions or crystal phase), Wang et al. used reduction precipitation method to fabricate Pd loaded three dimensionally ordered microporous (3DOM) In_2O_3 sensors, 0.5 wt% Pd

✉ Li Liu
liul99@jlu.edu.cn

✉ Yimin Gong
liweiy99@jlu.edu.cn

¹ College of Physics, State Key Laboratory of Superhard Materials, Jilin University, Changchun 130012, People's Republic of China

² Dehui Secondary Vocational Technical School, Changchun 130300, People's Republic of China

³ School of Materials Science and Engineering, Changchun University of Science and Technology, Changchun 130013, People's Republic of China

loaded 3DOM In_2O_3 sensor shows highest response (980 for 500 ppb NO_2) which is over 5 times higher than that of pure In_2O_3 at room temperature [12]. Minoo et al. fabricated Ga_2O_3 – In_2O_3 nanocomposite sensors via co-precipitation method, the results indicated that 10 wt% Ga_2O_3 – In_2O_3 and 25 wt% Ga_2O_3 – In_2O_3 sensors calcined at 500 °C show maximum response to ethanol and CO at 300 °C, respectively [13]. Rare earth metals as dopants into gas materials are of keen interest because of their high catalysis activity, highly conductive, high surface basicity and fast oxygen ion mobility, etc [14, 15]. For instance, Qin et al. have fabricated Er-doped In_2O_3 nanoribbon by carbon thermal reduction, and their ethanol sensing properties were significantly improved compared pure In_2O_3 [16]. In addition, Kapse et al. have prepared La-doped In_2O_3 cubic structure as H_2S sensor by a simple hydrothermal decomposition route, which indicated that doping of In_2O_3 with La^{3+} increases its response towards H_2S and 5.0 wt% La-doped In_2O_3 showed the maximum response at 125 °C [17].

Despite these exciting results, as far as we know few researches have been reported on formaldehyde sensitivity of In_2O_3 beaded-porous nanotubes (BPNTs), especially further introducing Tb dopant. In this work, we have further developed a new preparation method based on our previous research [18], and fabricated a new porous nanostructure by a simple regulatory mechanism. The process of forming BPNTs structure involves the separation of liquid phase with inverse polarity. The crystal phase, morphology and chemical composition of samples have been investigated and discussed. Furthermore, gas sensors base on fabricated samples response towards formaldehyde have been investigated and reported. Finally, the improved gas sensing properties of the Tb-doped In_2O_3 BPNTs were discussed based on the results from determination and characterization, and the enhanced gas sensing properties of the Tb-doped In_2O_3 BPNTs were also discussed and analyzed based on some reasonable gas sensing mechanism. Compared to other chemical compounds [6, 19–21]. Tb-doped In_2O_3 BPNTs exhibited the best sensing performance: high gas response, shorter response and recovery times, low limit of detection, good selectivity and long-term stability, etc. These excellent properties indicate that Tb-doped In_2O_3 BPNTs effective sensing material for the application of formaldehyde detection.

2 Experimental

2.1 Materials

Indium nitrate hydrate ($\text{In}(\text{NO}_3)_3 \cdot 4.5\text{H}_2\text{O}$, 99.9%, Sigma–Aldrich, USA), polyvinylpyrrolidone (PVP-K90, Mw = 1,300,000, Sigma–Aldrich, USA), terbium nitrate

hexahydrate ($\text{Tb}(\text{NO}_3)_3 \cdot 6\text{H}_2\text{O}$, 99%, Macklin, China), ethanol (99.5%, Aladdin, China), mineral oil (99.5%, Aladdin, China), *N,N* dimethylformamide (DMF, 99.5%, Aladdin, China) and were purchased and used without further purification.

2.2 Synthesis process

BPNTs were prepared by means of a simple process with two steps: electrospinning process followed by heat treatment. First of all, 0.2 g $\text{In}(\text{NO}_3)_3 \cdot 4.5\text{H}_2\text{O}$ and a certain amount of $\text{Tb}(\text{NO}_3)_3 \cdot 6\text{H}_2\text{O}$ (0 mol%, 2 mol%, 4 mol%, 6 mol% and 8 mol% of In atom) was dissolved in 2 g DMF and 4 g ethanol mixed solvent, 0.05 g mineral oil were added to the above mentioned solvent. The solution was agitated with a magnetic stirrer for an hour, add 0.3 g PVP to the solution and continue to stir it for further 12 h. After that, homogeneous precursor solution was moved into a plastic syringe with a metal spinneret. the positive and negative electrode of a high-voltage power supply was connected to the metal spinneret and a flat aluminum foil receiving plate respectively. the distance between the two electrodes was 25 cm, then 18KV direct current (DC) voltage was applied between the two poles. After 5 h of electrospinning, the as-collected nonwovens were placed into a muffle furnace and calcined (10°C/min) in air at 550 °C for 2 h to form In_2O_3 BPNTs. In addition, the pure In_2O_3 BPNTs and different atom percentage (2 mol%, 4 mol%, 6 mol% and 8 mol%) Tb-doped In_2O_3 BPNTs were expressed as Tb_0In , Tb_2In , Tb_4In , Tb_6In and Tb_8In , respectively.

2.3 Materials characterization

The phase structure of the samples was investigated via X-ray diffraction (XRD-6000 X-ray diffractometer, Shimadzu, Kyoto, Japan, with $\text{Cu K}\alpha$ radiation, $k = 1.5406 \text{ \AA}$). The surface morphology and chemical compositions of the samples were studied using field scanned electronic microscopy (FE-SEM, FEI Magellan 400, US), transmission electron microscopy (TEM, JEM-2200FS, JPN) and Energy dispersive spectroscopy attachment of FE-SEM (EDS, OXFORD, X-MAX150, UK). X-ray photoelectron spectroscopy (XPS, SSX-100 ESCA, USA) were applied for chemical binding analysis. The sensing properties were detected using an Intelligent gas-sensing analysis system (CGS-8, Beijing Elite Tech, CN). Stirrer (B11-3, SHANGHAI SILE, CN) and oven (KSL-1200X, HEFEI KEJING, CN) were used for mixing solution and calcining samples, respectively.

2.4 Fabrication and measurement of the gas sensors

In order to evaluate the gas sensibility of the prepared sensors, the gas properties of fabricated samples were researched by measuring variational resistance in air and target gas. The schematic of sensor device is shown in Fig. 1a, and the process of fabricating gas sensor is described as follows: Firstly, fabricated sample powder was mixed with deionized water in a weight ratio of 4:1 to form a homogeneous paste, then the obtained paste was uniformly spin-coated onto on the well cleaned alumina plates (thickness = 0.2 mm, area = 1.5 mm × 1.5 mm) (1000 rpm for 30 s), and the Au electrodes of sensor was coated. After that, the sensor was calcined (10°C/min) at 550 °C for 0.5 h to improve its stability for the measurement of sensing performance. Then the substrates were welded on the four feet socket. The gas concentration and flow was precisely controlled by mass flow controllers (MFC). During the test, the sensors are mounted in the insulating chamber. As diagrammed in Fig. 1b, The air carrier gas was used as the reference and flowed into the chamber (18 L).

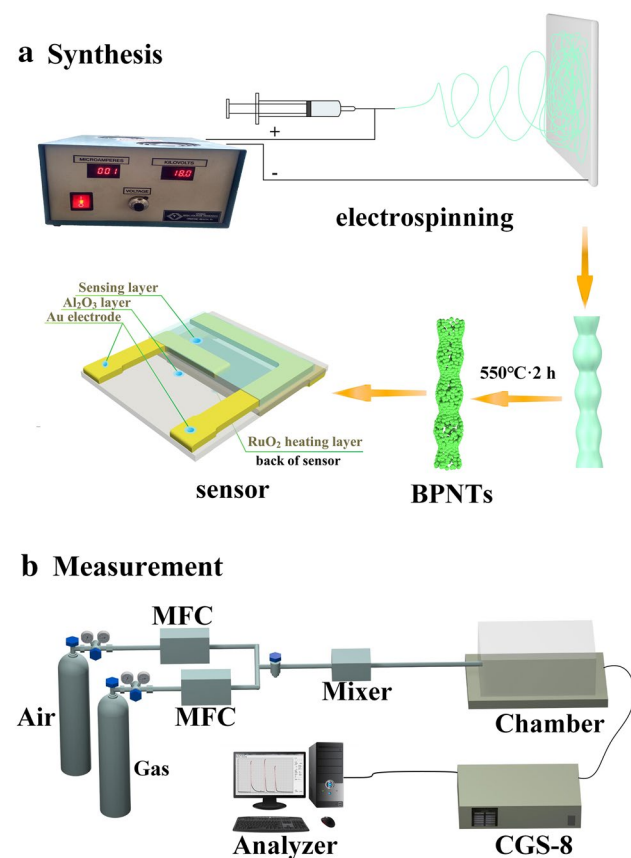


Fig. 1 **a** Schematic representation of gas sensor and diagram of synthesizing Tb_xIn ($x=0, 2, 4, 6, 8$) BPNTs and the structure of gas sensor; **b** schematic diagram of a set up for the gas characteristic measurement

The variety of target gases were introduced through valves and MFC to obtain the designed concentration. An appropriate amount of target gas was introduced into the closed chamber for measurement of the sensitive performance. When the sensor resistance reached new constant value, and the sensor was exposed to air again. Dynamic measurement system was coupled to the computer via a serial port cable, and the precise resistance signals from these sensing channels of test platform were received by computer in real time and processed by particular software (gas-sensing analysis system) automatically. In addition, the performance of the sensors was denoted by $S = R_g/R_a$, where R_a and R_g are the resistances of the sensors measured in air and in target gas, respectively. The sensor response and recovery time (τ_{res}/τ_{rec}) is defined as the time to reach 90% of the total resistance change. In order to ensure the data reliability, we performed 10 tests for every measurement.

3 Results and discussion

3.1 Crystalline structure

The crystal phases of pure and Tb-doped In_2O_3 BPNTs were investigated using X-ray diffraction with a scanning stepping angle of 0.02° in the 2θ range from 20° to 70° . The Rietveld refinements were performed on XRD data of synthesized samples using WinPLOTR program. As shown in Fig. 2. The diffraction peaks locating at $2\theta = 21.5^\circ, 30.58^\circ, 35.47^\circ, 45.7^\circ, 51.03^\circ$ and 60.68° correspond to (211), (222), (400), (431), (440), and (622) crystal planes of cubic bixbyite In_2O_3 (JCPDS No.06-0416), which is consistent with the data reported in literature [22]. It can be seen clearly from Fig. 2a that no peak for Tb_2O_3 detected when doping concentration is 2 mol%, 4 mol%, 6 mol% and 8 mol%, which may be attributed to the low dopant concentration. The result suggests that samples with low concentration form solid solution and host ions (In^{3+}) are replaced by dopant ions (Tb^{3+}). Another interesting observation is the broadening and shifting of peaks with an increase in dopant level in In_2O_3 lattice (Fig. 2b). Peak shifting slightly toward lower diffraction angle in doped samples. According to the Prague equation, it is because that Tb ionic (1 \AA) with large radii incorporated into the In_2O_3 crystal and replaced the smaller In ionic (0.81 \AA) sites [23]. Whereas the broadening of peak and the weakening of peak strength can be ascribed to the effect of decreased crystallite size and stain existing in In_2O_3 [23]. According to the Debye–Scherrer and Williamson Hall (WH) plot [24–28], the crystallite size (D) and strain could be calculated:

$$D = \frac{0.9\lambda}{\beta \cos \theta} \quad (1)$$

$$\frac{\beta \cos \theta}{\lambda} = \frac{k}{d} + \frac{4\epsilon \sin \theta}{\lambda} \quad (2)$$

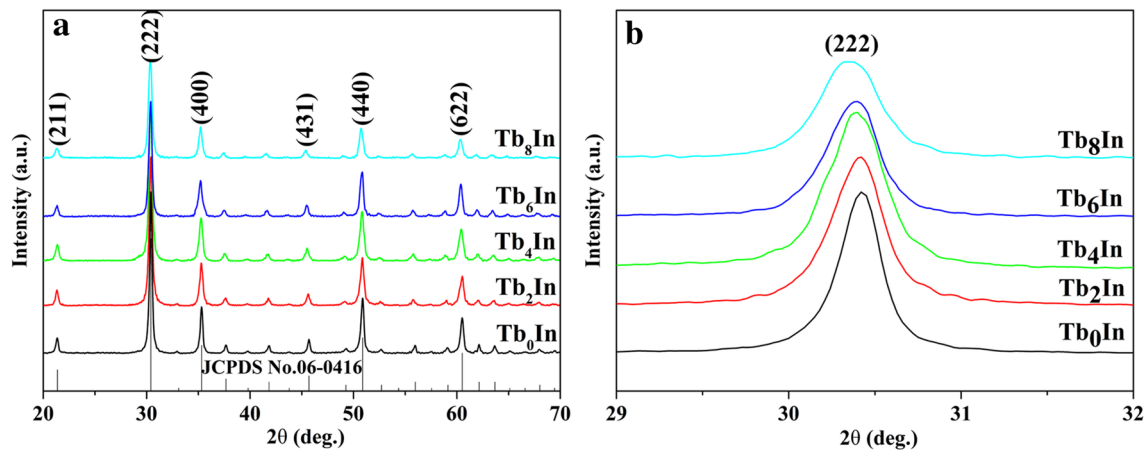


Fig. 2 XRD patterns of the different contents of Tb-doped In_2O_3 samples after annealing

Table 1 Crystal parameters (a), Crystallite size (D) calculated from Scherrer's formula (D_s) and WH plot (D_w), Strain (ϵ) of samples

Sample	Crystal parameters, a (Å)	Crystallite size, D (nm)		Strain $\epsilon \cdot 10^{-3}$
		D_s	D_w	
Tb ₀ In	10.112	14	14.8	0.11
Tb ₂ In	10.125	11.4	12.4	1.54
Tb ₄ In	10.131	10.7	11.1	1.62
Tb ₆ In	10.135	9.05	10.3	1.79
Tb ₈ In	10.137	7.54	8.9	2.33

Where λ is the X-ray wavelength, θ is the Bragg's diffraction angle, β is the full width at half maxima and D and d is the crystallite size, k is Scherrer's constant ($k = 0.9$), ϵ is micro-strain in crystal. For calculating the strain of lattice, $4\sin\theta/\lambda$ and $\beta\cos\theta/\lambda$ correspond x and y axis, respectively. and the micro-strain is calculated from the slope of the graph fitted by a straight line. Besides, some Tb^{3+} may be positioned on an interstitial lattice site (a-site or c-site) [29, 30], which can further enhance defect concentration of samples. The enhancement will be discussed later. The lattice parameter 'a' is also calculated by the Bragg's law. These results are summarized in Table 1. The strain and lattice constant 'a' become larger with the increase of dopant content. Specifically, in a In_2O_3 unit cell, 8 and 24 indium atoms are situated at b-sites at d-sites, respectively, and 48 oxygen atoms occupy e-sites, no atom occupies a-sites or c-sites (a-site: an octahedral position for the sublattice of the six d-site indium atoms; c-site: a tetrahedral position for the sublattice of one b-site and three d-site indium atoms) [29, 31]. When the dopant ions substitute the In^{3+} ions of the host matrix, they should experience either a distorted or compressed octahedral environment. In addition, the trend of crystallite size according to the

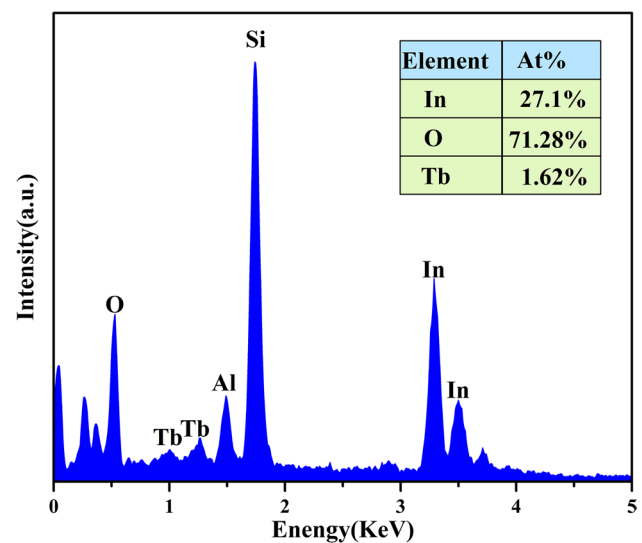


Fig. 3 EDS spectra of Tb₆In

two equation is similar (decreasing with increasing dopant level). The gain size values (D_w) are larger than that (D_s) calculated by using the Scherrer formula. The difference is due to the broadening effect [24]. In general, the crystal structure of In_2O_3 is not significantly changed after introducing Tb element. As for XRD result, the above analysis shows that Tb dopant just change some crystal parameter and crystallite size of materials and these changes will improve the gas sensitivity obviously according to previous reports [32].

Meanwhile, the chemical compositions of Tb₆In sample were obtained by EDS (Fig. 3), and the measured results are agreement with expectations (the indium, terbium and oxygen elements), which demonstrates that the Tb element existences in the In_2O_3 structures. The Al and Si elements are caused by aluminum sample stage, silicon wafer.

3.2 Morphological analysis

The morphologies and structures of the pure and Tb-doped In_2O_3 BPNTs were further investigated by TEM. Before annealing, we take Tb_6In sample as an example (Fig. 4a), globular mineral oil dispersed homogeneously in the inner of nanofibers and form beaded nanowires. After annealing, the structure of pure and Tb-doped In_2O_3 BPNTs are shown in Fig. 4b–f. The morphologies of Tb-doped In_2O_3 almost show no change compared to that of pure In_2O_3 , they all possess an average diameter of about 160 nm, and their tube walls are easily recognizable. In addition, TEM and HRTEM have been used to make clear the formation of BPNTs. From Fig. 4g, the BPNTs structure of Tb_6In can be clearly presented by TEM image, which gets a good agreement with the FE-SEM results. The HRTEM image of Tb_6In (Fig. 4h) displays that the interplanar spacing between two adjacent lattice planes of about 0.41 nm and 0.29 nm, which is attributed to the (211) and (222) plane of cubic bixbyite In_2O_3 , respectively. The spotted ring-like SAED pattern of Tb_6In is given in Fig. 4i, the rings also can be assigned (211), (222), (400) and (622) planes of cubic bixbyite In_2O_3 .

On the basis of our previous theoretical analysis [18], the precursor is a multiphase complex solution consisting of polar solvents (ethanol, DMF) Nonpolar liquid (mineral oil), polymer binder (PVP) and nitrates ($\text{In}(\text{NO}_3)_3$ and $\text{Tb}(\text{NO}_3)_3$). This experiment shows that nitrates can dissolve in mixed solvent completely. However, mineral oil in the form of small droplets is dispersed in solution. PVP is dissolved in mixed solvent, which makes the precursor have viscosity (1230 cp). After stirring, the result is that the precursor is milk white and can be preserved stably for a long time. The formation of In_2O_3 BPNTs is shown in Fig. 1. Before electrospinning, mineral oil exists in two forms: small liquid drop and molecule, and they are dispersed evenly in precursor solution after stirring. The precursor solution possesses viscosity due to the PVP, which can stabilize nonpolar mineral oil and not occur phase separation. Nevertheless, after electrospinning, these small liquid drops or molecules of mineral oil gradually aggregate into bigger liquid drops and form uniform beaded nanowires, as we can see from Fig. 4a. This performance is possibly because the surface energy of nanowires is higher than precursor solution, and small liquid drops or molecules tend to gather together in bigger liquid drops for reducing surface energy in core. During thermal

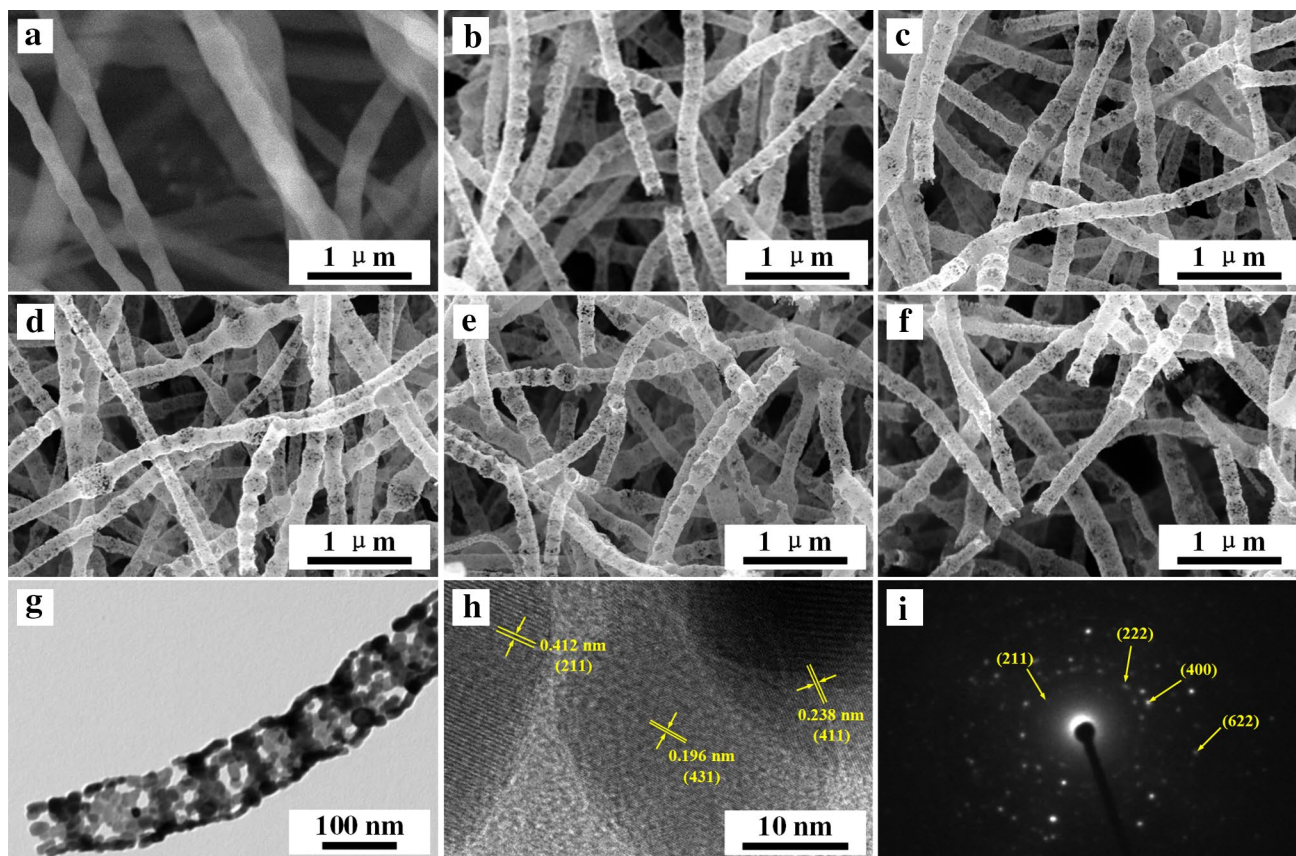


Fig. 4 FE-SEM images of samples (a–f). a Tb_6In before annealing. b–f Tb_0In , Tb_2In , Tb_4In , Tb_6In , Tb_8In BPNTs. g low resolution image, h high resolution TEM (HRTEM) image and i SEAD pattern of Tb_6In BPNTs

treatment with the heating rate of 15 °C, these liquid drop of mineral oil which server as a template will evaporate and expand with heat quickly. Along with Kirkendall effect [33], the ordered porous structure was formed in the surface of beads.

To confirm the chemical compositions and oxidized states of elements, the survey scan and high resolution scan of X-ray photoelectron spectroscopy (XPS) analysis was also carried out, as shown in Fig. 5. Taking Tb_6In as an example, the survey scan spectrum of Tb_6In reveals the photo emission peaks of In, O, C and Tb, and peak of any impurities were not seen in all spectrum, which indicates the high purity of samples and was line in the results of EDS. Figure 5b shows the In 3d spectra, the two strong peaks corresponding to In $3d_{5/2}$ and In $3d_{3/2}$ are centered in 444.24 and 451.80 eV, respectively, and it's spin orbit splitting is about 7.56 eV, which indicate the indium element exists in the form of In^{3+} [6]. Figure 5c displays the Tb 4d spectra of Tb_6In BPNTs in 146.9 eV, which confirms the presence of Tb^{3+} oxidation state [23].

The O 1s spectrum is used to confirm the presence of oxygen vacancy in Fig. 5d. The oxygen O1s peak for all samples is resolved into three peaks namely O-1, O-2 and O-3 and they are centered at 530, 531.6 and 532.7 eV, respectively. O-1 peak corresponds to O^{2-} ions bounded with In^{3+} . O-3 peak is often caused by absorbed oxygen such as O_2^- , O^- ,

H_2O . While peak labeled as O-2 is ascribed to oxygen vacancy which appear in all the samples [12]. And the percent contents of O-2 peak reflects the concentration of oxygen vacancies. We calculated the O-2 ratio by $O-1/(O-1+O-2+O-3)$, $O-3/(O-1+O-2+O-3)$, and $O-3/(O-1+O-2+O-3)$ [6], and the results were listed in Table 2. It is found that the percent of O-2 peak in Tb_6In BPNTs is higher than other samples, which signifies that Tb_6In has maximum number of oxygen vacancies. The results indicated that introducing moderate amounts of Tb can increase oxygen vacancy. According to previous research [29], One possible reason is that some Tb^{3+} serving as interstitial ions are position at a-site or c-site. According to Kröger-Vink notation, the phenomenon can be explained by the following equation:

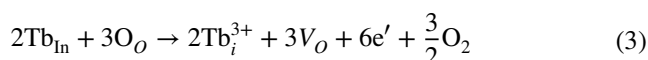
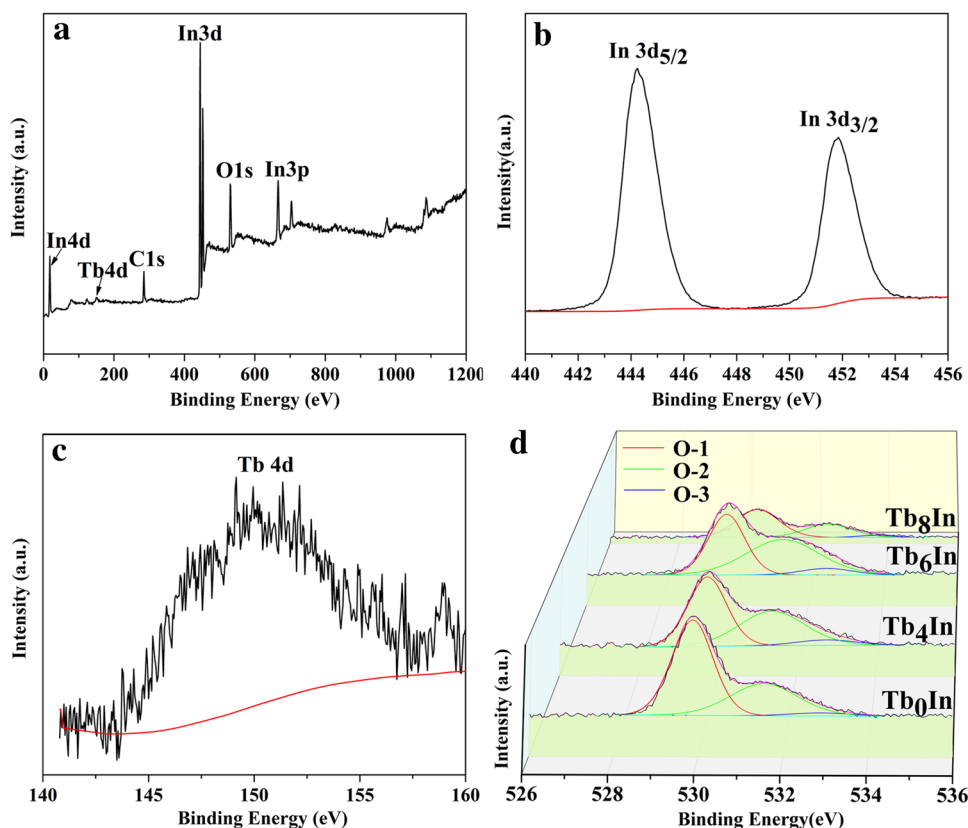


Table 2 Percent contents of O-1, O-2, and O-3 in various samples

Samples	O 1s		
	O-1	O-2	O-3
Tb_0In	62.44	34.52	3.04
Tb_4In	51.31	42.75	5.94
Tb_6In	43.30	50.30	6.40
Tb_8In	53.83	38.00	8.17

Fig. 5 a Survey, b In 3d, c Tb 3d XPS spectra of Tb_6In ; d O 1s XPS spectra of Tb_xIn ($x=0, 4, 6, 8$)



Compared with In^{3+} , these Tb^{3+} located at In^{3+} position have larger ionic radii, and maybe more easily move to a-site or c-site. And many studies have demonstrated that oxygen vacancy severing as active sites play a pivotal role in gas sensing process [8, 12, 32].

3.3 Gas sensing studies

It is well known that the sensing properties of semiconductor oxide gas sensor are highly dependent on its operating temperature, which is because of the temperature dependence of adsorption/desorption kinetics [34]. Therefore, to explore the optimum working temperature, Fig. 6a shows that the response of the as-fabricated sensors toward 50 ppm formaldehyde changes with operating temperature ranging from 120 to 200 °C. The response value of the sensor increases with the increase in sensor temperature and attains maximum value at 160 °C, however, further increasing temperature will lead to the decreases of response value. Therefore, the optimum operating temperature of all sensors are 160 °C,

and the temperature is used to further study the sensing properties of sensors. This phenomenon can be explained as the adsorption and desorption kinetics on the surface of gas sensing materials. Generally, the lower chemical activation of In_2O_3 results in the deficient reaction between target gas and adsorbed O_2 at low temperatures [32]. When increasing working temperature achieve a threshold value, a balance between the acceleration of reduction reaction and desorption of O_2 molecules will be built, and the response value reaches the maximum. However, if temperatures continue to rise and beyond the threshold value, the built balance will be destroyed, and the desorption process of O_2 molecules have a dominating position, which will cause the decrease of the response. In addition, the dependence of sensors specific response on different Tb concentrations was tested at 160 °C toward 50 ppm formaldehyde. In addition, the response increases quickly with increasing content of Tb, and the response reach maximum value at concentration of 6 mol%. While the response gradually decreases with further increasing Tb content. The behavior results from

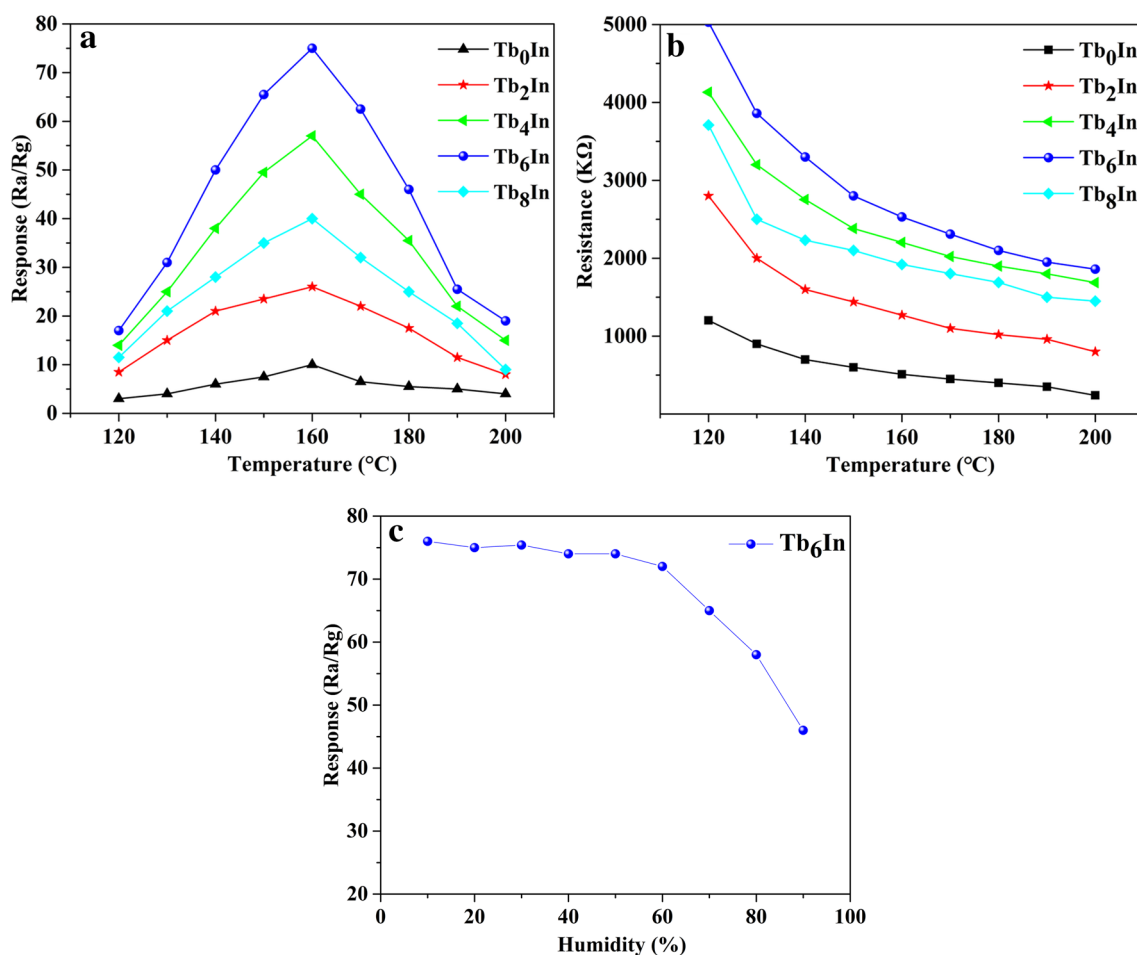


Fig. 6 The response values (a) and resistance R_a (b) of sensors as a function of the working temperature for 50 ppm formaldehyde, c the effect of humidity on the response of Tb_6In to 50 ppm formaldehyde at 160 °C

the decrease of active sites [32, 35]. Moderate doping concentration of Tb can generate more active sites or oxygen vacancies, which will obviously increase the response of sensors. However, excessive dopant will reduce these active sites and then cause the lower response values. The result can be confirmed from XPS. On the other hand, the decrease in crystallite size due to the increase of dopant concentration (confirmed from XRD) provides a large number of adsorption sites for gas and then improves response [7].

Figure 6b shows the dependence of sensor resistance on temperature and Tb doping concentration in air. It can be seen that the resistance of all sensors is decreased with a rise of temperature, this is because of the thermal excitation of electrons and desorption of oxygen species, which is agree with the electrical characteristics of semiconductor oxide and other research [35]. In addition, it is noted that the resistance is enhanced with the increasing Tb doping concentration at the same temperature. the behavior may result from the lattice defect and more O₂ absorbed on surface of samples [36].

The effect of humidity on the gas sensitivity has also been investigated. The sensitivity of the sensor to formaldehyde at different relative humidity is shown in Fig. 6c. The response is relatively stable in the humidity range of 20–60%. However, response value drops sharply when the humidity exceeds 60%. The result reveals that it is necessary for the sensor of Tb₆In BPNTs to detect formaldehyde under lower relative humidity. To ensure the stability and higher response of sensor, the relative humidity kept constant 25% for all test.

Figure 7a presents the dynamic response/recovery transient curves of pure and Tb-doped In₂O₃ BPNTs toward various concentrations from 10 to 200 ppm (insert shows In₆In from 100 to 500 ppb) of formaldehyde at 160 °C. As shown

in Fig. 7a, the response values of all sensors are increased gradually with the increased concentration. In addition, the sensors based on Tb₆In BPNTs shows a maximum response value toward all the different concentrations gas, which is about eight times larger than that of sensors based on Tb₀In BPNTs. Particularly for Tb₆In response in low concentration, the response can reach to about 1.27 toward 100 ppb of formaldehyde. In a practical application, the response and recovery time are important parameters for evaluating performance of gas sensor. Figure 7b presents the correlation of Log(S – 1) versus Log(C) by means of the linear fit, where S and C is the response value and the concentration of the formaldehyde, respectively. It is shown that the calculated correlation coefficient (R²) of gas sensor based on Tb₂In BPNTs is about 0.9994, which indicates a good linearity. Actually, the good linearity can help reducing the cost and complexity of the embedded circuit design [39].

Figure 8a shows the repeatability of the Tb₆In gas sensor toward 50 ppm formaldehyde at 160 °C. Clearly, the curves shows that the baseline can keep level after several successive sensing cycles, which indicate that the sensor have a good reversibility and repeatability.

The response and recovery time of different contents of Tb-doped In₂O₃ gas sensors to 50 ppm formaldehyde at 160 °C is listed in Table 3. The response and recovery times of all sensors were less than 3 s and 15 s. It is worth noting that the gas sensor based on Tb₆In BPNTs shows a short response and recovery time of 2 s and 10 s at 160 °C, respectively. the result may be attributed to the porous structure of samples which may help the diffusion of air and target gas.

A comparison of formaldehyde sensing performance between this work and previously reported sensors is summarized in Table 4. It can be seen that the sensor fabricated in this work shows outstanding or even superior sensing

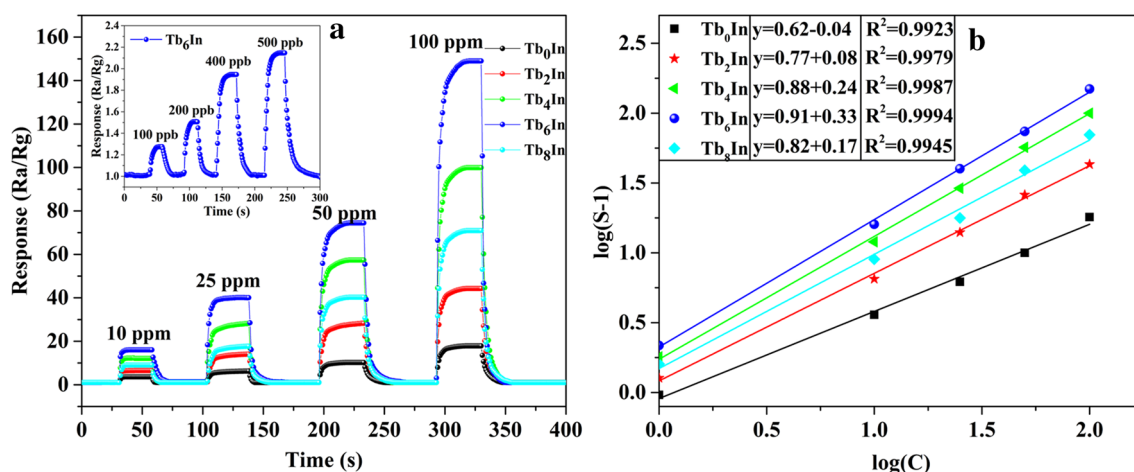


Fig. 7 a The dynamic responses of sensors to 0.1–100 ppm formaldehyde gas at 160 °C. b Logarithm plots of response value versus the gas concentration at 160 °C

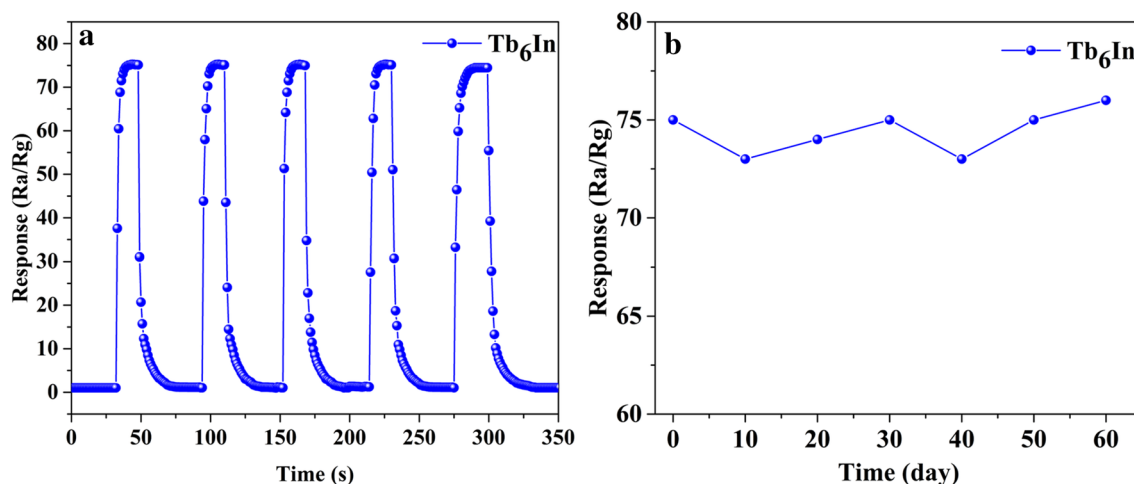


Fig. 8 a Reproducibility and b long-term stability of Tb₆In gas sensor at 160 °C

Table 3 The response and recovery time of all samples toward 50 ppm formaldehyde

Samples	Response time (s)	Recovery time (s)
Tb ₀ In	3	14
Tb ₂ In	2	13
Tb ₄ In	3	12
Tb ₆ In	2	12
Tb ₈ In	4	15

performances, including high response, fast response/recovery speed and lower operating temperature.

The gas sensing selectivity is one of the key parameter to evaluate the sensing ability of semiconductor materials. Figure 9 shows a function of gas response to 50 ppm of various gases such as formaldehyde, acetone, methanol and carbon monoxide, benzene, methylbenzene. As a result, the sensor based on Tb₆In shows a higher response to all target gases than any other sensors, and exhibits highest response toward formaldehyde and are almost insensitive to other gases at 160 °C. The result indicates that sensor based on Tb₆In shows an excellent selectivity for formaldehyde. In addition, the long-term stability of the Tb₆In BPNTs gas sensor to 50 ppm formaldehyde is also exhibited in Fig. 8b,

During the whole test period, the response value almost keep unchanged and the measured deviation of response value is within 2.7%, which demonstrating the good long-term stability of the sensor.

It is acknowledged that the gas sensing mechanism of gas sensor based on semiconducting metal oxide is explained as the resistance change of samples which is caused by the adsorption and desorption of oxygen. As shown in Fig. 10. When sensor is exposed to air, O₂ in the surrounding air will be adsorbed on the surface of In₂O₃ and meanwhile capture electrons from the conduction band of In₂O₃, as a result, these chemisorbed oxygen species will be existed as oxygen species (O²⁻, O⁻, O₂⁻). The chemical equations of oxygen adsorption are represented as follows:



Then a depletion layer is created on the surface of the materials, and the resistance of materials will be increased (Fig. 10). Once the formaldehyde is introduced, the target gas

Table 4 Comparison of the sensing performances toward formaldehyde between sensors reported in the literatures and the present study

Materials	C (ppm)	T (°C)	Response	$\tau_{\text{res}}/\tau_{\text{rec}}$ (s)	LOD (ppm)	Refs.
ITO NTs	100	160	24.5	2.6/79.4	–	[6]
Fe-doped In ₂ O ₃ hollow microspheres	50	260	7.31	6/3	1	[37]
Porous Ga _{0.6} In _{1.4} O ₃ nanofibers	100	150	52.4	14/25	0.2	[38]
SnO ₂ -graphene	100	260	35	–	–	[19]
Ordered mesoporous NiO	100	300	11	119/39	0.2	[20]
Hollow SnO ₂ nanofibers	100	120	32	25/104	0.5	[21]
Tb ₆ In BPNTs	50	160	75	2/12	0.1	This work

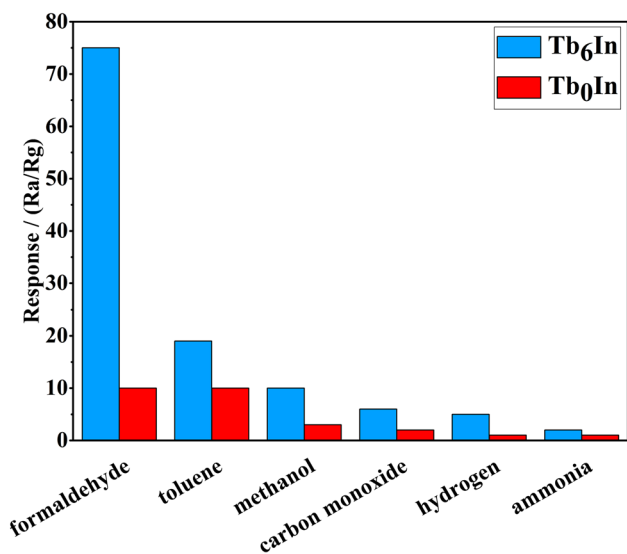
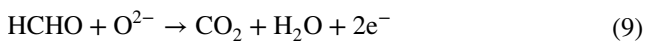
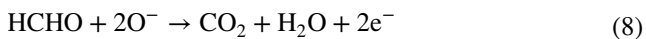


Fig. 9 The responses of Tb₆In and Tb₀In to 50 ppm different gases at 160 °C

will react with adsorbed oxygen ion and release electrons back to conduction band, which result in decreased resistance of sensor. The process of the reaction is shown below:



The significant enhanced response of Tb₆In may be because of the following reasons: Firstly, decreasing crystallite size is an effective way to enhance the response of gas sensor, this is because smaller crystallite can provide more gas adsorption sites [40]. In this work, the growth of samples is inhibited after introducing Tb dopant (confirmed from XRD). Secondly, it is reported that surface basicity can affect the process of gas sensing reaction [41]. rare earth oxide are basic oxides, the surface basicity of samples will be increased after doping Tb, and then enhance the sensor response towards target gas. Thirdly, oxygen vacancies, used as preferential adsorption sites for gas molecules, play a key role in the process of gas sensing [42]. In air, V_O can provide electrons for adsorbed oxygen and become V_OV_O [43]. The measured result of XPS indicate that the number of oxygen vacancies increases with increase in Tb concentration (≤ mol%). The Tb dopant can introduce new energy level (E_v below the In₂O₃ conduction band) according to previous reports [4, 32]. The electrons in the donor level near conduction band can jump into the conduction band easily at working temperature (160 °C), and then facilitate more oxygen absorbed on the surface in the form of oxygen ions. As a result, the surface will form a wider depletion layer than pure In₂O₃ and samples shows higher resistance in air. Finally, because of the differences in ionic radii of In³⁺ and Tb³⁺, lattice strain and distortion will be form in the crystal structures (confirmed form XRD), which improve interaction between target gas and sensor surface active sites resulting in high response values. Of course, the special porosity

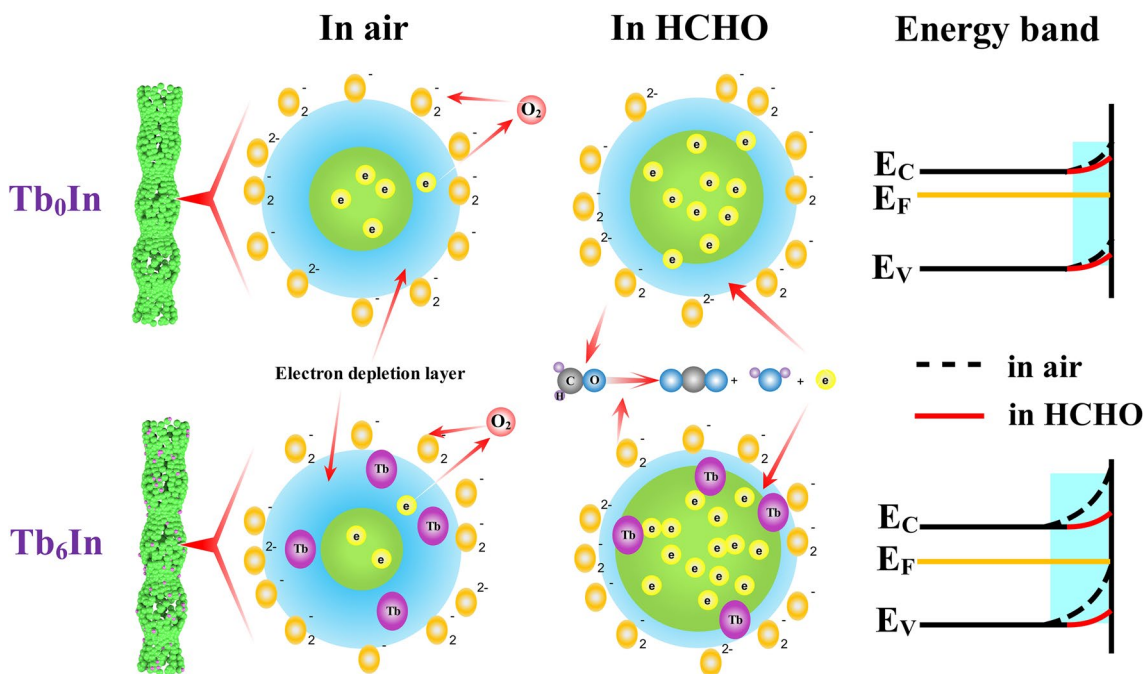


Fig. 10 Schematic diagram of the possible mechanism for Tb₀In and Tb₆In exposed to air and formaldehyde

structure is the basis for high response of the gas sensor. the structure not only provides large surface area for oxygen or target gas, but also plenty of channel for the rapid diffusion of gases.

4 Conclusion

In summary, the pure and Tb-doped In₂O₃ BPNTs were synthesized by electrospinning. Mineral oil serving as a template reagent plays a key role in the formation of BPNTs structure. Morphological analysis result shows that a mass of small holes distribute in the beads of nanotubes. XRD and XPS results indicated that Tb³⁺ introducing into the crystal lattice of In₂O₃ lead to a lattice distortion and more oxygen vacancies. After a series of gas sensing measurements, the Tb₆In exhibited the highest specific response, lower LOD, fast response/recovery time, good selectivity and long-term stability to formaldehyde gas. And the significantly improved gas sensing properties were mainly resulted from the enriched defects caused by doping Tb and the special beads porous hollow structures. This research would give a simple method for the BPNTs structure and an effective sensing material for the application of formaldehyde detection.

Acknowledgements The work has been supported by the Jilin Provincial Science and Technology Department (No. 20170101199JC).

References

1. A. Jamshidi, Y. Hajizadeh, M.M. Amin et al., *J. Chem. Technol. Biotechnol.* **93**, 1328 (2017). <https://doi.org/10.1002/jctb.5496>
2. D.J. Luecken, S.L. Napelenok, M. Strum, R. Scheffe, S. Phillips, *Environ. Sci. Technol.* **52**, 4668 (2018). <https://doi.org/10.1021/acs.est.7b05509>
3. R.J. Mendelsberg, G. Garcia, H. Li, L. Manna, DJ Milliron, *J. Phys. Chem. C* **116**, 12226 (2012). <https://doi.org/10.1021/jp302732s>
4. S. Ghosh, K. Das, G. Sinha, J. Lahtinen, SK De, *J. Mater. Chem.* **1**, 5557 (2013). <https://doi.org/10.1039/C3TC31087F>
5. K. Anand, J. Kaur, R.C. Singh, R. Thangaraj, *Chem. Phys. Lett.* **670**, 37 (2017). <https://doi.org/10.1016/j.cplett.2016.12.057>
6. J.Y. Zhou, J.L. Bai, H. Zhao et al., *Sens. Actuators B Chem.* **265**, 273 (2018). <https://doi.org/10.1016/j.snb.2018.03.008>
7. A. Katoch, Z.U. Abideen, J.-H. Kim, S.S. Kim, *Sens. Actuators B Chem.* **232**, 698 (2016). <https://doi.org/10.1016/j.snb.2016.04.013>
8. C. Zhao, B. Huang, E. Xie, J. Zhou, Z. Zhang, *Sens. Actuators B Chem.* **207**, 313 (2015). <https://doi.org/10.1016/j.snb.2014.10.087>
9. J. Wang, J. Su, H. Chen, X. Zou, G.-D. Li, *J. Mater. Chem.* **6**, 4156 (2018). <https://doi.org/10.1039/C8TC00638E>
10. X. Chen, L. Li, W. Zhang et al., *J. Mol. Catal. A: Chem.* **414**, 27 (2016). <https://doi.org/10.1016/j.molcata.2015.12.023>
11. J. Ma, H. Fan, H. Tian et al., *Sens. Actuators B Chem.* **262**, 17 (2018). <https://doi.org/10.1016/j.snb.2018.01.226>
12. Z. Wang, G. Men, R. Zhang, F. Gu, D. Han, *Sens. Actuators B Chem.* **263**, 218 (2018). <https://doi.org/10.1016/j.snb.2018.02.105>
13. M. Bagheri, A.A. Khodadadi, A.R. Mahjoub, Y. Mortazavi, *Sens. Actuators B Chem.* **220**, 590 (2015). <https://doi.org/10.1016/j.snb.2015.06.007>
14. V. Kumar, O.M. Ntwaeaborwa, J. Holsa, D.E. Motaung, H.C. Swart, *Opt. Mater.* **46**, 510 (2015). <https://doi.org/10.1016/j.optmat.2015.05.011>
15. S. Singh, A. Singh, B.C. Yadav, P.K. Dwivedi, *Sens. Actuators B Chem.* **177**, 730 (2013). <https://doi.org/10.1016/j.snb.2012.11.096>
16. Z. Qin, Y. Liu, W. Chen et al., *Chem. Phys. Lett.* **646**, 12 (2016). <https://doi.org/10.1016/j.cplett.2015.12.054>
17. V.D. Kapse, S.A. Ghosh, G.N. Chaudhari, F.C. Raghuwanshi, D.D. Gulwade, *Vacuum* **83**, 346 (2008). <https://doi.org/10.1016/j.vacuum.2008.05.027>
18. D. Haojie, Y. Lei, H. Yue et al., *Mater. Res. Express* **4**, 095022 (2017). <https://doi.org/10.1088/2053-1591/aa89f9>
19. Y. Cao, Y. Li, D. Jia, J. Xie, *RSC Adv.* **4**, 46179 (2014). <https://doi.org/10.1039/C4RA06995A>
20. X. Lai, G. Shen, P. Xue et al., *Nanoscale* **7**, 4005 (2015). <https://doi.org/10.1039/C4NR05772D>
21. D. Wang, M. Zhang, Z. Chen et al., *Sens. Actuators B Chem.* **250**, 533 (2017). <https://doi.org/10.1016/j.snb.2017.04.164>
22. A. Montazeri, F. Jamali-Sheini, *Sens. Actuators B Chem.* **242**, 778 (2017). <https://doi.org/10.1016/j.snb.2016.09.181>
23. A. Hastir, N. Kohli, R.C. Singh, *Sens. Actuators B Chem.* **231**, 110 (2016). <https://doi.org/10.1016/j.snb.2016.03.001>
24. S.P. Choudhury, N. Kumari, A. Bhattacharjee, *J. Mater. Sci. Mater. Electron.* **28**, 18003 (2017). <https://doi.org/10.1007/s10854-017-7743-3>
25. G.K. Williamson, W.H. Hall (1953) *Acta Metal.* **1**: 22. [https://doi.org/10.1016/0001-6160\(53\)90006-6](https://doi.org/10.1016/0001-6160(53)90006-6)
26. M. Rahimi-Nasrabadi, M. Behpour, A. Sobhani-Nasab, M.R. Jeddy, *J. Mater. Sci. Mater. Electron.* **27**, 11691 (2016). <https://doi.org/10.1007/s10854-016-5305-8>
27. A. Ziarati, A. Sobhani-Nasab, M. Rahimi-Nasrabadi, M.R. Ganjali, A. Badii, *J. Rare Earths* **35**, 374 (2017). [https://doi.org/10.1016/S1002-0721\(17\)60922-0](https://doi.org/10.1016/S1002-0721(17)60922-0)
28. M. Rahimi-Nasrabadi, M. Behpour, A. Sobhani-Nasab, S. Mostafa Hosseinpour-Mashkani, *J. Mater. Sci. Mater. Electron.* **26**, 9776 (2015). <https://doi.org/10.1007/s10854-015-3648-1>
29. T. Tomita, K. Yamashita, Y. Hayafuji, H. Adachi, *Appl. Phys. Lett.* **87**, 051911 (2005). <https://doi.org/10.1063/1.2001741>
30. G.B. González, T.O. Mason, J.P. Quintana et al., *J. Appl. Phys.* **96**, 3912 (2004). <https://doi.org/10.1063/1.1783610>
31. GB González (2012) *Materials* **5**: 818. <https://doi.org/10.3390/ma5050818>
32. A. Hastir, N. Kohli, R.C. Singh, *J. Phys. Chem. Solids* **105**, 23 (2017). <https://doi.org/10.1016/j.jpcs.2017.02.004>
33. Y. Yin, R.M. Rioux, C.K. Erdonmez, S. Hughes, G.A. Somorjai, A.P. Alivisatos, *Science* **304**, 711 (2004). <https://doi.org/10.1126/science.1096566>
34. A. Hastir, R.L. Opila, N. Kohli et al., *J. Mater. Sci.* **52**, 8502 (2017). <https://doi.org/10.1007/s10853-017-1059-9>
35. H. Gao, Q. Yu, S. Zhang et al., *Sens. Actuators B Chem.* **269**, 210 (2018). <https://doi.org/10.1016/j.snb.2018.04.161>
36. M.W. Ahn, K.S. Park, J.H. Heo, J.G. Park, *Appl. Phys. Lett.* **93**, 263103 (2008). <https://doi.org/10.1063/1.3046726>
37. R. Dong, L. Zhang, Z. Zhu, J. Yang, X. Gao, S. Wang, *Cryst. Eng. Commun.* **19**, 562 (2017). <https://doi.org/10.1039/C6CE02061E>
38. H. Chen, J. Hu, G.-D. Li, Q. Gao, C. Wei, X. Zou, *ACS Appl. Mater. Interfaces.* **9**, 4692 (2017). <https://doi.org/10.1021/acsami.6b13520>

39. L. Qin, J. Xu, X. Dong et al., *Nanotechnology* **19**, 185705 (2008). <https://doi.org/10.1088/0957-4484/19/18/185705>
40. J. Wang, B. Zou, S. Ruan, J. Zhao, F. Wu, *Mater. Chem. Phys.* **117**, 489 (2009). <https://doi.org/10.1016/j.matchemphys.2009.06.045>
41. M. Bagheri, N.F. Hamedani, A.R. Mahjoub, A.A. Khodadadi, Y. Mortazavi, *Sens. Actuators B Chem.* **191**, 283 (2014). <https://doi.org/10.1016/j.snb.2013.10.001>
42. C. Zhao, G. Zhang, W. Han et al., *Cryst. Eng. Commun.* **15**, 6491 (2013). <https://doi.org/10.1039/C3CE40962G>
43. S. Xu, J. Gao, L. Wang et al., *Nanoscale* **7**, 14643 (2015). <https://doi.org/10.1039/C5NR03796D>